Supporting information

Supporting text I

1 Experimental

1.1 Materials and chemicals

Bismuth nitrate pentahydrate ($Bi(NO_3)_3 \cdot 5H_2O$), hydrogen peroxide (H_2O_2, 30%), ammonium hydroxide ($NH_3 \cdot H_2O$, 25%−28%), and potassium bromide (KBr) were purchased from Sinopharm Chemical Reagent Co., Ltd. In addition, Shanghai Macklin Biochemical Co., Ltd supported Gold(III) chloride hydrate ($HAuCl_4 \cdot 4H_2O$) and ammonium hexafluorotitanate ($(NH_4)_2TiF_6$). Wuhan Huaxiang Kejie Biotechnology Co., Ltd. provided sodium ethyl xanthate (SEX), sodium butyl xanthate (SBX), sodium isoamyl xanthate (SIAX), and sodium isopropyl xanthate (SIPX).

1.2 Microstructure characterization

The crystal phase structure of the samples was confirmed by X-ray diffraction (XRD, XRD-7000). The morphology of the samples was observed by using scanning electron microscope (SEM, Hitachi S-4800) and transmission electron microscope (TEM, JEM-F200). The thermogravimetric (TG) analysis was characterized by using an analyzer (STA-8000). The surface area of the samples was investigated by Brunauer-Emmett-Teller (BET, Quadrasorb SI). An X-ray photoelectron spectroscope (XPS, NexsaG2, Thermo Scientific) was applied to investigate the compositions and valence state of the elements of the obtained photocatalysts. Liquid chromatography-mass spectrometry (LC-MS, Agilent 1290 Infinity & Agilent G6125B) was applied to measure the mass/charge ratio (*m*/*z*) to determine the intermediate products. Electrochemical workstation (CHI760E) was used to draw Nyquist EIS plots to interpret carrier transfer efficiency.

1.3 Preparation of Au-BiOBr-TiO_2 composites

Figure S1 illustrates the three-stage method for the synthesis of the AuBT ternary composites, involving hydrothermal, water bath, and photodeposition steps. Firstly, TiO_2 (T) was synthesized through a hydrothermal process whereby 1.5 g of $(NH_4)_2TiF_6$ and an appropriate amount of H_2O_2 were added to 50 mL of deionized water. After adjusting pH to 8 with ammonia and stirring for 30 min, the precursor solution was transferred to a Teflon-lined stainless-steel autoclave and kept at 160 °C for 12 h, the obtained precipitate was dried and subjected to calcination at 400 °C. Then, binary composites of BiOBr-TiO_2 (BT) were prepared via a water bath method by homogenizing 1 mmol TiO_2 and 0.05 mmol $Bi(NO_3)_3 \cdot 5H_2O$ using a short-time stirring. Finally, a KBr solution was gradually added to achieve Br:Bi elemental ratio of 1:1. The mixture was then kept at 50 °C for 2 h before being washed and dried. The preparation method of BiOBr (B) was the same as that of BT, except TiO_2 was not added.

For AuBT ternary composites, Au and binary composites were constructed by photodeposition. First, 1.21 mmol of BT binary composites was added to 50 mL of deionized water and stirred vigorously for 5 min to obtain slurry I. Second, 1 g of $HAuCl_4 \cdot 4H_2O$ was dissolved in 100 mL of deionized water to obtain a 24.28 mmol/L $HAuCl_4 \cdot 4H_2O$ aqueous solution and set as solution II. A certain amount of solution II was added to slurry I and sonicated and stirred for 5 min, respectively. Following that, the mercury lamp was activated and the mixture was steadily stirred for an additional 30 min. Furthermore, the resulting sample was washed several times and dried. Finally, the dried samples were calcined at a certain temperature (200, 300, 400, 500 and 600 °C) for 2 h to obtain the expected AuBT ternary composites. The samples with Au molar ratio of 0.2%, 0.4%, 0.6% and 0.8% were defined as AuBT-1, AuBT-2, AuBT-3 and AuBT-4, respectively. The preparation method of Au-TiO_2 (AuT) and Au-BiOBr (AuB) were the same as that of AuBT, except BiOBr and TiO_2 were not added, respectively.

2.4 Measurement of photocatalytic activity

The photocatalytic apparatus was a reaction infrastructure containing circulating cooling water, 50 mL quartz tubes, 400 W xenon lamp, etc. To ensure that the catalytic reaction was not affected by thermal catalysis, the cooling water system kept the reaction temperature below 20 °C. The xenon lamp provided the light source. The quartz tubes were responsible for the loading of different concentrations of SEX solution and different dosages of photocatalyst. Dark adsorption was maintained for 30 min before photocatalytic reaction for achieving adsorption-desorption dynamic equilibrium accompanied by aeration and magnetic stirring. During the dark adsorption and photocatalytic reaction stage, 5 mL of the suspension was quickly extracted and filtered to separate the SEX solution and photocatalyst. The concentration of SEX solution was then analyzed by UV-Vis spectrophotometer for characteristic peaks. The maximum peak of SEX solution was located at 301 nm. Following the Lamber-Beer law, the degradation ratio D could be calculated by Eq. (S1).

$$D=\frac{C_0-C_t}{C_0}=\frac{A_0-A_t}{A_0}\times 100\% \qquad \text{(S1)}$$

The first order kinetic result showed the linear relationship between $\ln(C_0/C_t)$ and the reaction time t, which could be calculated by Eq. (S2).

$$\ln\left(\frac{C_0}{C_t}\right)=kt \qquad \text{(S2)}$$

where A_0, A_t and C_0, C_t were the absorbance values and concentrations of SEX solution at reaction times of 0 and t, respectively; k was the primary reaction rate constant.

Supporting text II

Synthesis conditions have been shown to significantly influence the performance of photocatalysts. Series of experiments specifically explore the role of Au loading and calcination temperature as two critical parameters. To objectively investigate the properties of the samples, the adsorption capacity and degradation efficiency of SEX molecules are used as benchmark indices. During the experiments, the visible light intensity was set as 400 W, the initial concentration of SEX was 20 mg/L, and the amount of catalyst was 0.2 g/L. Figures S6(a) and (b) depict the curves of degradation efficiency and degradation kinetics of different composites to SEX. As shown in Figure S6(a), no significant reduction on the concentration of SEX is observed in the blank test, suggesting that xanthate molecules remain stable under light conditions without photocatalyst. The adsorption-desorption equilibrium of SEX over the photocatalyst in the dark reaction is achieved in 30 min. After activation of the light reaction, the degradation efficiency of TiO_2 and AuT to SEX is exceptionally low. This outcome indicates that TiO_2 and AuT have a limited competence to degrade SEX due to their inefficient utilization of visible light. On the other hand, BiOBr, AuB and BT are more effective in degrading SEX. Furthermore, the degradation efficiencies of AuB and BT surpass that of BiOBr, indicating that BiOBr exhibits excellent performance when combined with the host catalyst TiO_2, and also contributes significantly to the catalytic degradation reaction when paired with the co-catalyst Au. Compared to other samples, the adsorption and degradation performance of AuBT ternary composites towards SEX are significantly enhanced, indicating that the coexistence of Au, BiOBr, and TiO_2 greatly promotes both adsorption and photocatalytic degradation. This can be attributed to the beneficial synergistic effect among the three components and the formation of heterojunctions. With an increase in Au loading, a trend of increasing then decreasing in the degradation reaction constant of AuBT to SEX is observed. Specifically, the highest degradation rate of 0.12666 min^{-1} is obtained for AuBT-3, which mainly benefits from a strong correlation between the adsorption percentage and catalytic reaction rate. Furthermore, combined with characterization results of these composites, AuBT-3 shows excellent dispersity of each component and a large specific surface area which can generate more active sites and thus promote rapid photodegradation reactions. Therefore, AuBT-3 is determined to have the optimal Au loading capacity and is therefore utilized in subsequent experiments.

The calcination temperature has a significant effect on the physical phase and crystalline form of AuBT, which in turn affects the degradation reaction rate. Figures S6(c) and (d) show the degradation curves and pseudo primary reaction kinetic constant curves of AuBT composites at different calcination temperatures. After the dark reaction process, SEX molecules reach an adsorption-desorption dynamic equilibrium. In the photocatalytic stage, the photocatalytic efficiency gradually increases over the catalysts with the calcination temperature increasing from 200 to 300 °C, and a maximum degradation efficiency of 95.2% is obtained. This is primarily due to the crystallization improvement of each component with increasing temperature. However, when the calcination temperature continues to increase beyond 300 °C, the degradation efficiency of AuBT composites to SEX decreases, until reaching 57.38% at 600 °C. The SEM characterization results in Figures S7(a)−(e) reveal that there is no notable change in the sample morphology at the calcination temperatures of 200 and 300 °C. Nevertheless, as the temperature increases further, a decrease in the representative layer structure of BiOBr in SEM images is clearly observed, indicating the disappearance of BiOBr at high temperatures. The TG curve in Figure S8 shows that there is a mass loss of 1.21% before 440 °C, because composites lost adsorbed water. Furthermore, as shown in Figure S2(d), there is a mass loss of 6.03% from 440 to 800 °C due to loss of bound water and the decomposition of BiOBr into $Bi_{24}O_{31}Br_{10}$ and Br_2 gas.

Supporting text III

Carefully selecting application parameters for photocatalysts is crucial in industrial applications. The applicability of AuBT composites was assessed by investigating the photocatalyst dosage, xanthate concentration, optimal wastewater pH, degradation feasibility of different types of xanthate, recycling performance. The photocatalytic degradation and kinetic curves of AuBT-3 composites with different dosages to SEX molecule are shown in Figures S9(a) and (b). The addition of AuBT composites is taken as the only variable, which is set from 0.1 to 0.3 g/L, and all SEX degradation processes follow a first-order kinetic equation. In Figure S9(a), with the increase of the photocatalyst dosage, the adsorption performance gradually increases. However, all samples reach adsorption-desorption dynamic equilibrium in 30 min. The photocatalytic rate increases first and then decreases with the further increase of photocatalyst dosage. When the dosage of the photocatalysts adds from 0.1 to 0.2 g/L, the degradation rate increases due to the enhanced active sites. When it further increases to 0.25 g/L and 0.3 g/L, due to the rapid reaction in the first 10 min and reaching near equilibrium degradation (reaching 93.16% and 94.73% respectively), the degradation rate sharply declined in the latter 10 min. Therefore, a single first-order reaction kinetics curve is insufficient to describe the entire reaction process. Excessive use of photocatalysts can lead to waste of resources and may block visible light and reduce the intensity of light. At a dosage of 0.2 g/L of AuBT-3, the photocatalytic degradation rate can reach as high as 95.2%, which corresponds to the larger pseudo-first-order reaction rate constant achieved. Therefore, it can be concluded that 0.2 g/L of photocatalyst is an optimal condition for further optimization.

The concentration of xanthate discharged into wastewater ranges from approximately 10 to 30 mg/L [4−5]. Consequently, experiments in this chapter are conducted using simulated mineral wastewater containing xanthate ions at concentrations ranging from 10 to 30 mg/L, and the corresponding photodegradation results are displayed in Figures S9(c) and (d). As the SEX concentration increases, the adsorption properties of photocatalysts gradually approach saturation, causing a reduction in the photodegradation kinetic constant. When the SEX concentration is below 20 mg/L, it is difficult to accurately describe the primary reaction kinetics with a single kinetic curve. This is because the first 10 min of degradation results in an equilibrium being reached, with degradation percentage of 10 and 20 mg/L pollutant concentration reaching 94.89% and 93.51%, respectively. This decreases the probability of interaction between the pollutant and the material, leading to a decrease in the degradation rate. When SEX concentration is above 20 mg/L, the kinetic constant decreases as the concentration increases. This suggests that the fixed dosage of AuBT-3 composites is unable to maintain the same rate of catalytic degradation for an excess amount of pollutants. When the concentration of SEX is in the range of 10 to 30 mg/L, the photocatalytic effect of AuBT-3 is highly significant, resulting in a degradation rate exceeding 90%. Considering the subsequent experimental conditions, an SEX concentration of 20 mg/L was chosen as the most suitable condition due to its optimal degradation rate.

Supporting text V

The exchange and correlation energies were characterized by the Perdew-Burke-Ernzerhof (PBE) functional, which describes a generalized gradient approximation (GGA) [9−10]. The method proposed by HUJO et al [11], using standard parameters, is utilized to describe the weak dispersion interaction. The ionic cores are described by ultrasoft pseudopotentials, and the BFGS algorithm is used to evaluate the potential energy surface during optimization [12]. The structure optimization is fully relaxed until convergence criteria are met. Particularly, energy and force are set as 1×10^{-5} eV and 0.02 eV/Å, respectively. For structure relaxations, the first Brillouin zone of such a slab sampled with the Monkhorst-Pack mesh with 5×5×1 grids is used. Besides, a denser 9×9×1 k-point grids are further employed to obtain a more accurate electronic property computation. To avoid interactions under periodic boundary conditions, a vacuum space of 15 Å along *z* axial is set. To evaluate the interaction strength between the substrate and the adsorbed SEX molecule, the following calculation equation of adsorbed energy (E_{ad}) is used.

$$E_{\text{ad}} = E_{\text{Total}} - E_{\text{SEX}} - E_{\text{sub}} \qquad \text{(S3)}$$

where E_{SEX} and E_{sub} represent the energies of the free SEX molecule and the BT substrate, respectively; E_{Total} represents the total energy of the SEX molecule adsorbed on BT substrate.

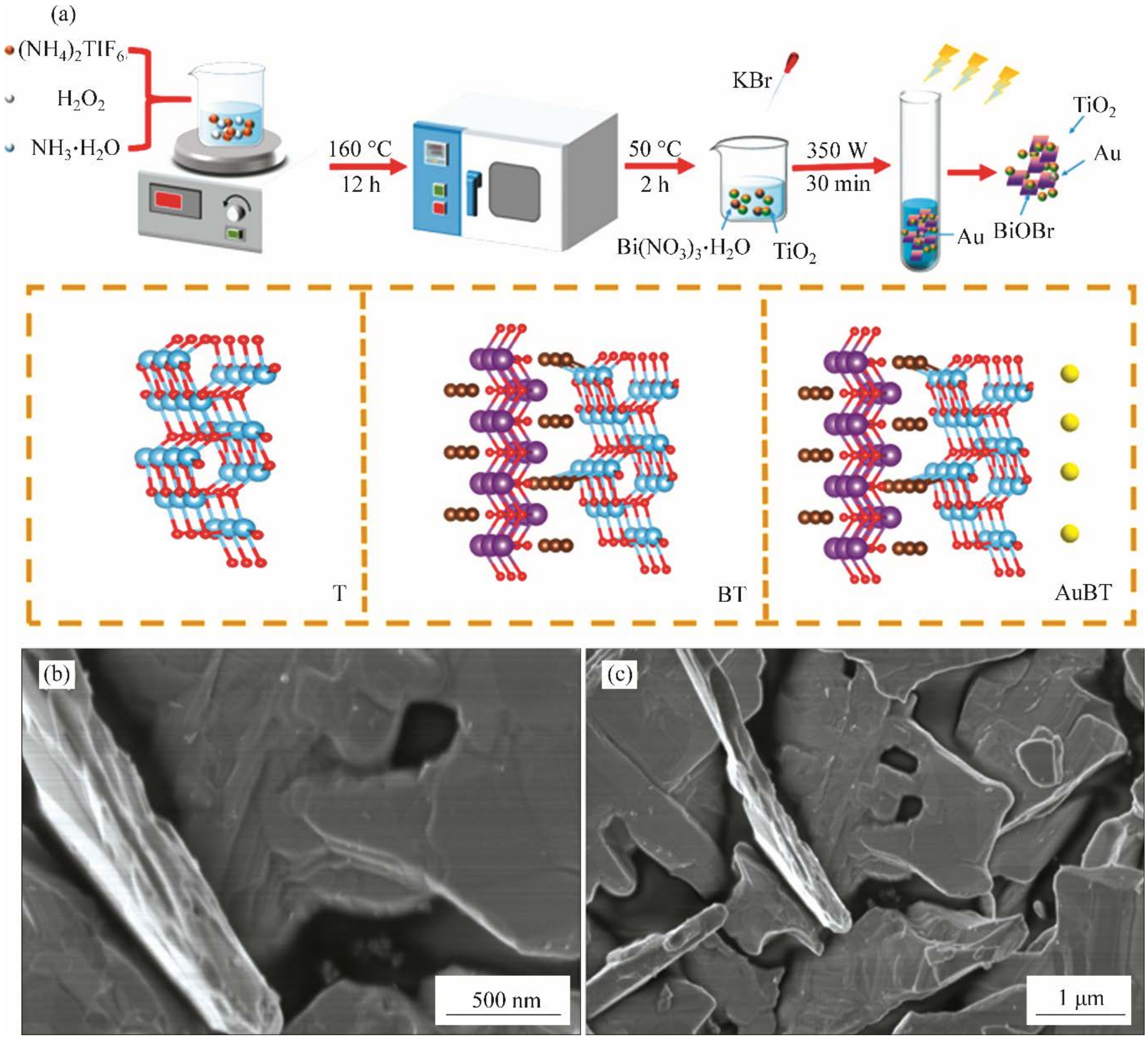

Figure S1 (a) Schematic illustration of synthesis process of AuBT composites; (b) SEM image of $Bi_{24}O_{31}Br_{10}$

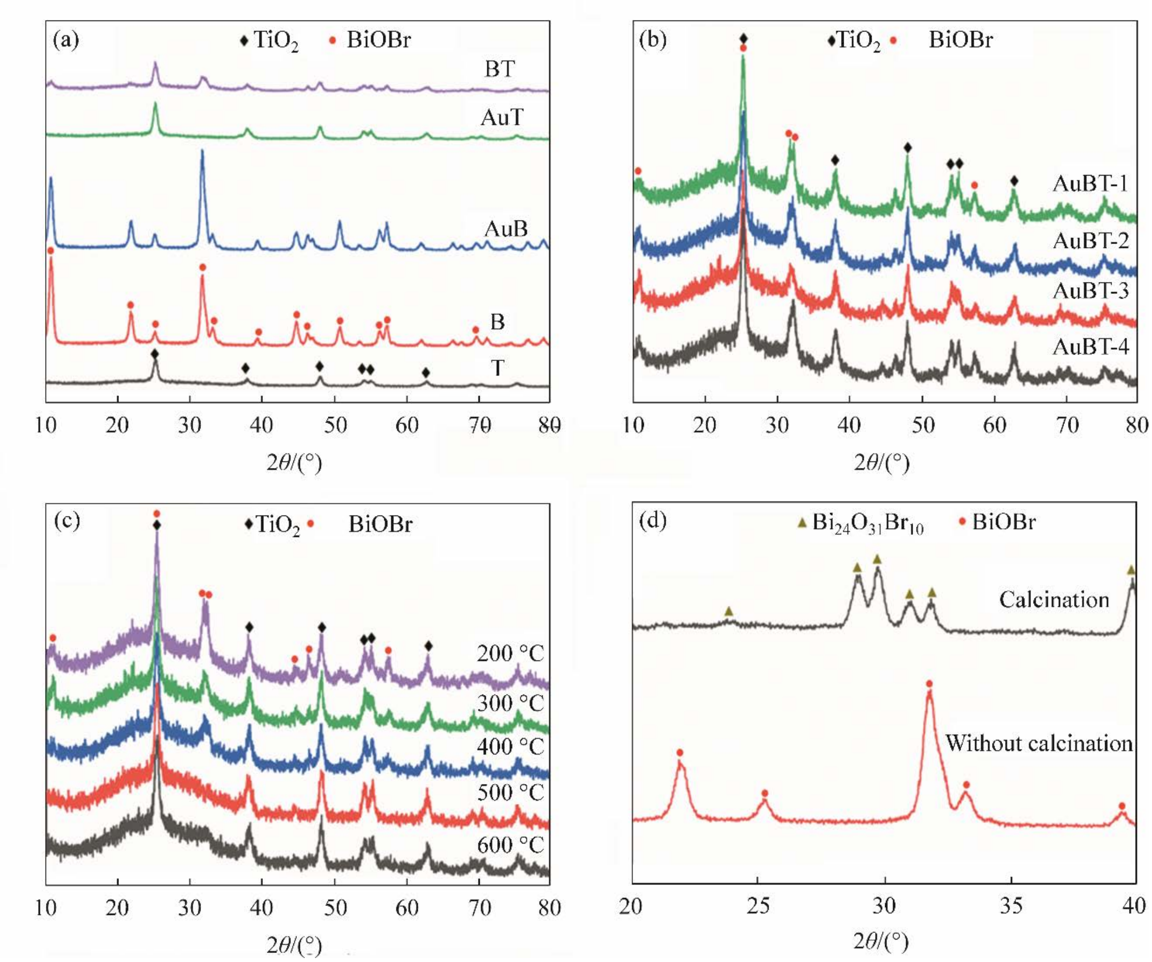

Figure S2 XRD patterns of different samples: (a) T, B, AuB, AuT and BT; (b) AuBT composites with different Au loading amounts; (c) AuBT-3 composites annealed at different calcination temperatures; (d) BiOBr samples before and after calcination at 600 °C

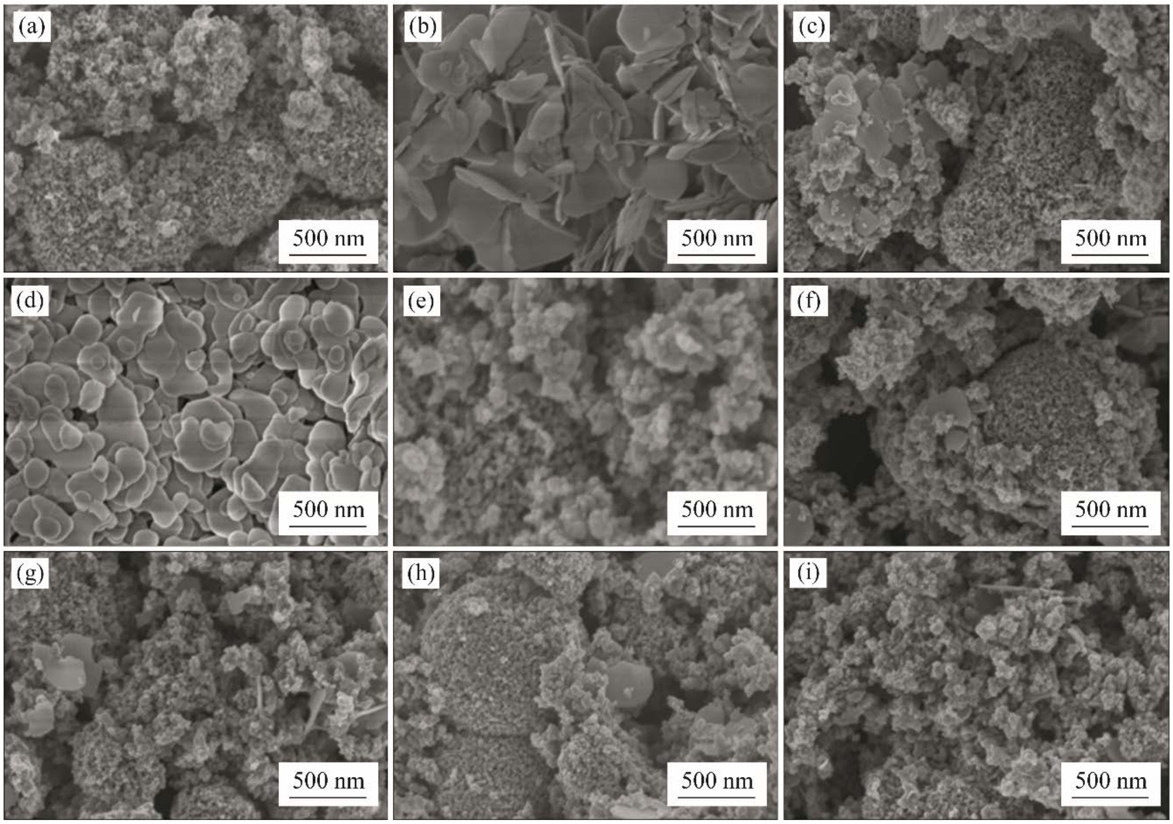

Figure S3 SEM images of different samples: (a) T; (b) B; (c) BT; (d) AuB; (e) AuT; (f) AuBT-1; (g) AuBT-2; (h) AuBT-3; (i) AuBT-4

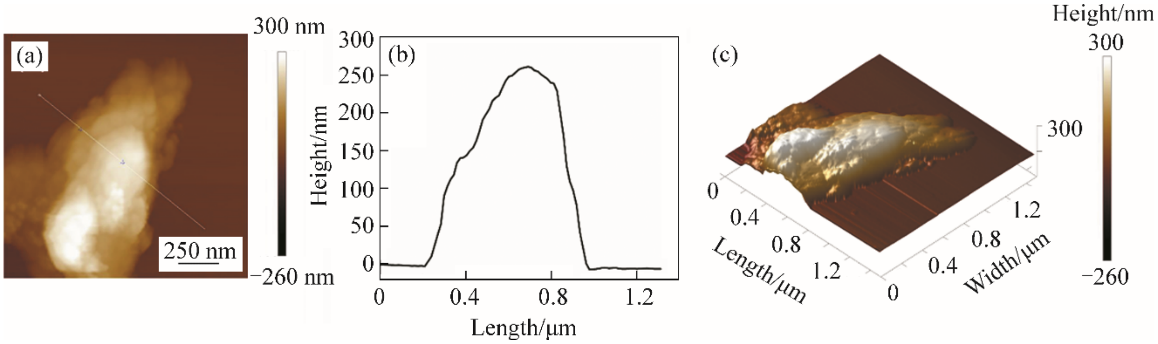

Figure S4 AFM typical analysis results of AuBT-3 composites: (a) AFM images; (b) Height profile of the line in the AFM image; (c) Three-dimensional structure view

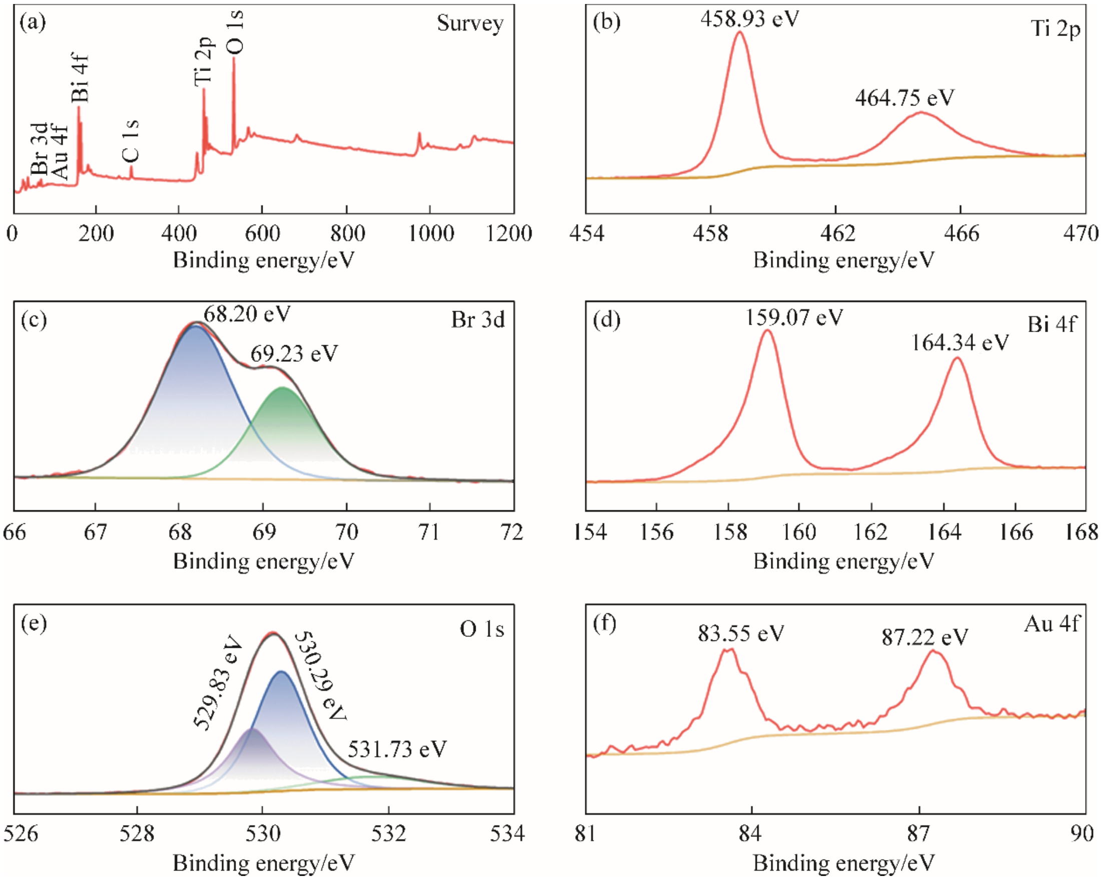

Figure S5 XPS spectra of AuBT-3 composites: (a) Survey scan; (b)Ti 2p; (c) Br 3d; (d) Bi 4f; (e) O 1s; (f) Au 4f

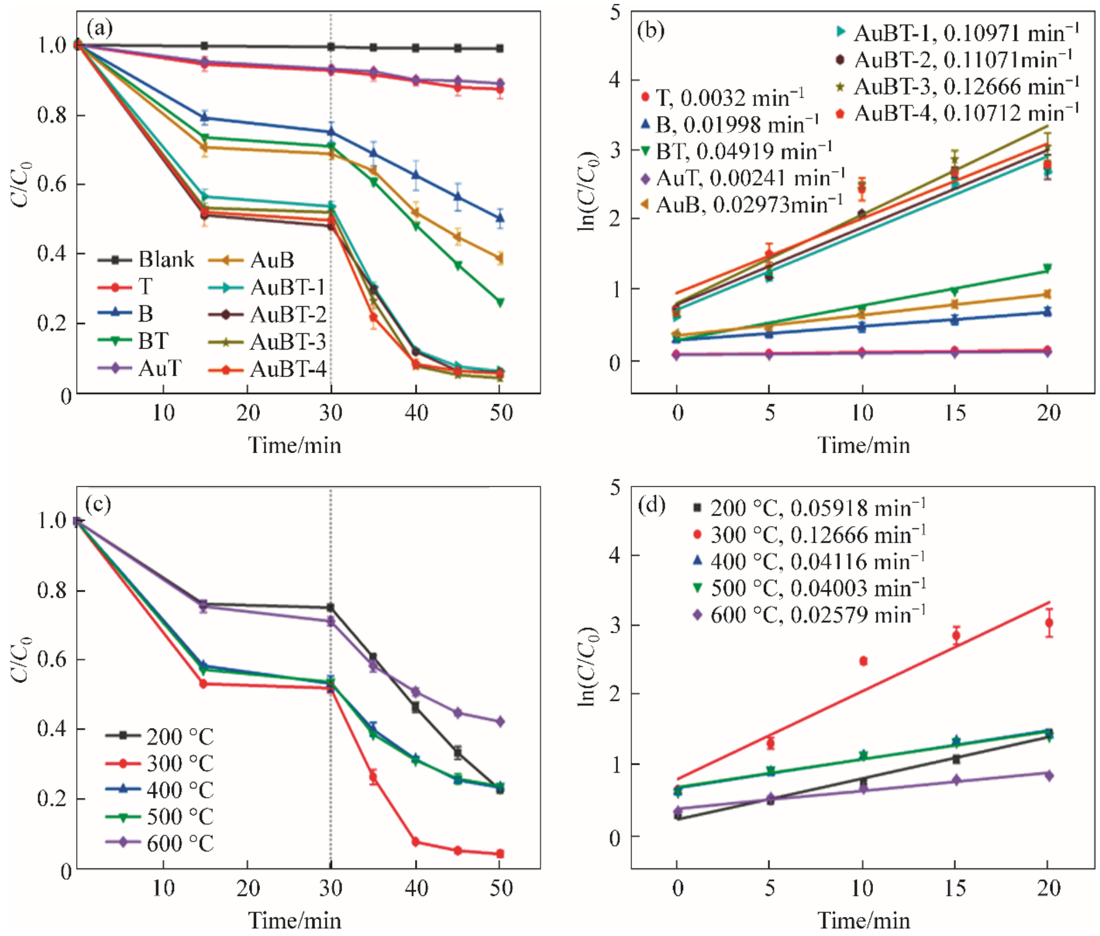

Figure S6 (a) Degradation efficiency curves and (b) kinetic curves of different samples to 20 mg/L SEX; (c) Degradation efficiency curves and (d) kinetic curves of AuBT-3 composites annealed at different calcination temperatures to 20 mg/L SEX

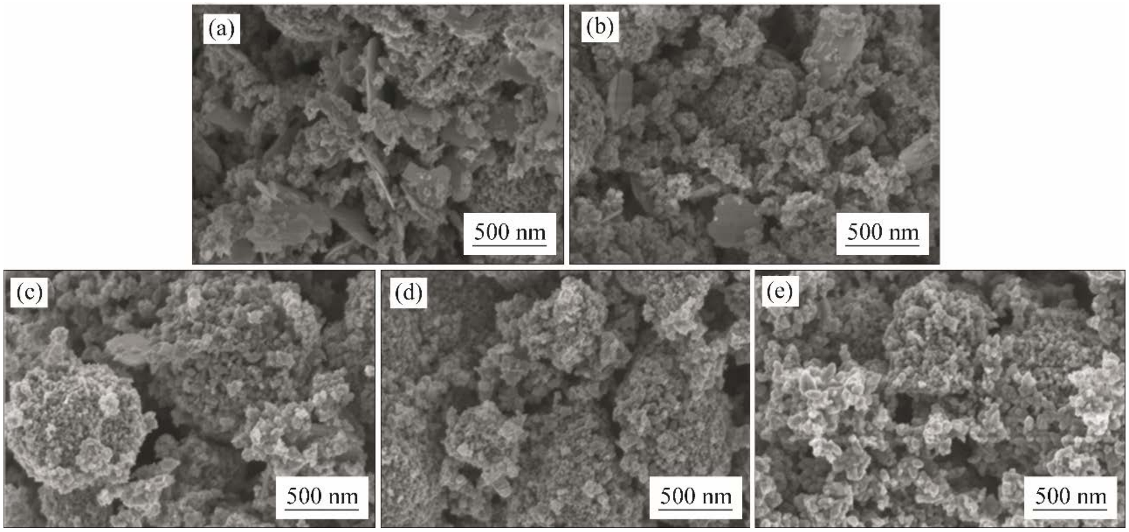

Figure S7 SEM images of AuBT composites synthesized at different calcination temperatures: (a) 200 °C; (b) 300 °C; (c) 400 °C; (d) 500 °C; (e) 600 °C

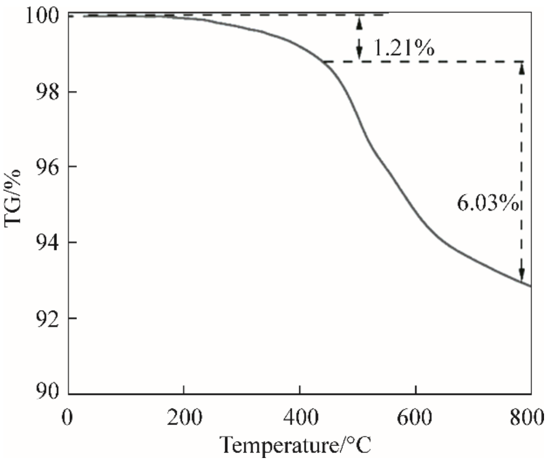

Figure S8 TG curve of AuBT composites

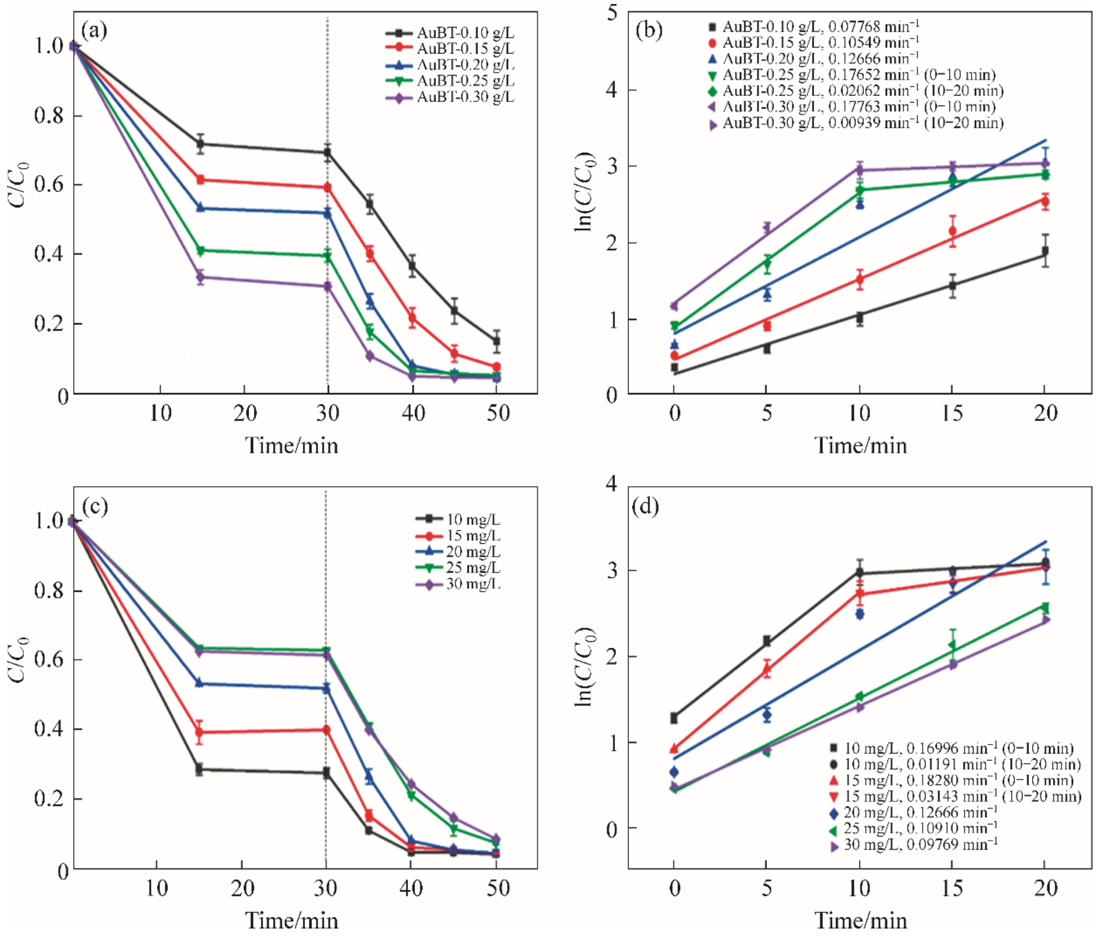

Figure S9 (a) Degradation efficiency curves and (b) kinetic curves of AuBT-3 composites with different dosages to 20 mg/L SEX; (c) Degradation efficiency curves and (d) kinetic curves of AuBT-3 composites to various initial concentrations of SEX

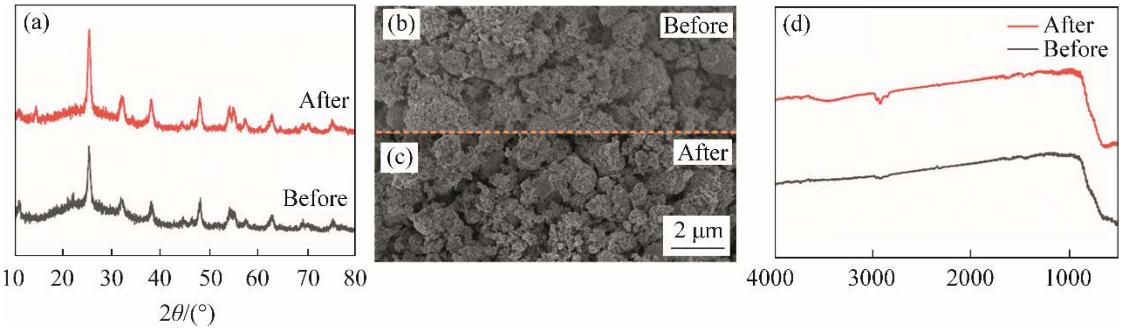

Figure S10 (a) XRD patterns, (b−c) SEM images and (d) FTIR spectra of AuBT-3 composites before and after photocatalytic degradation reaction

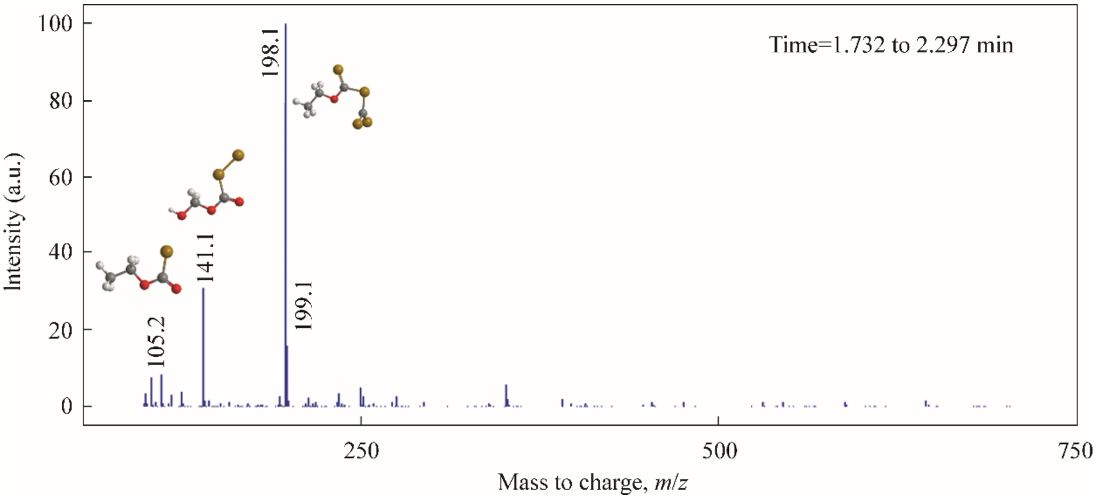

Figure S11 LC-MS results of photocatalytic degradation of SEX

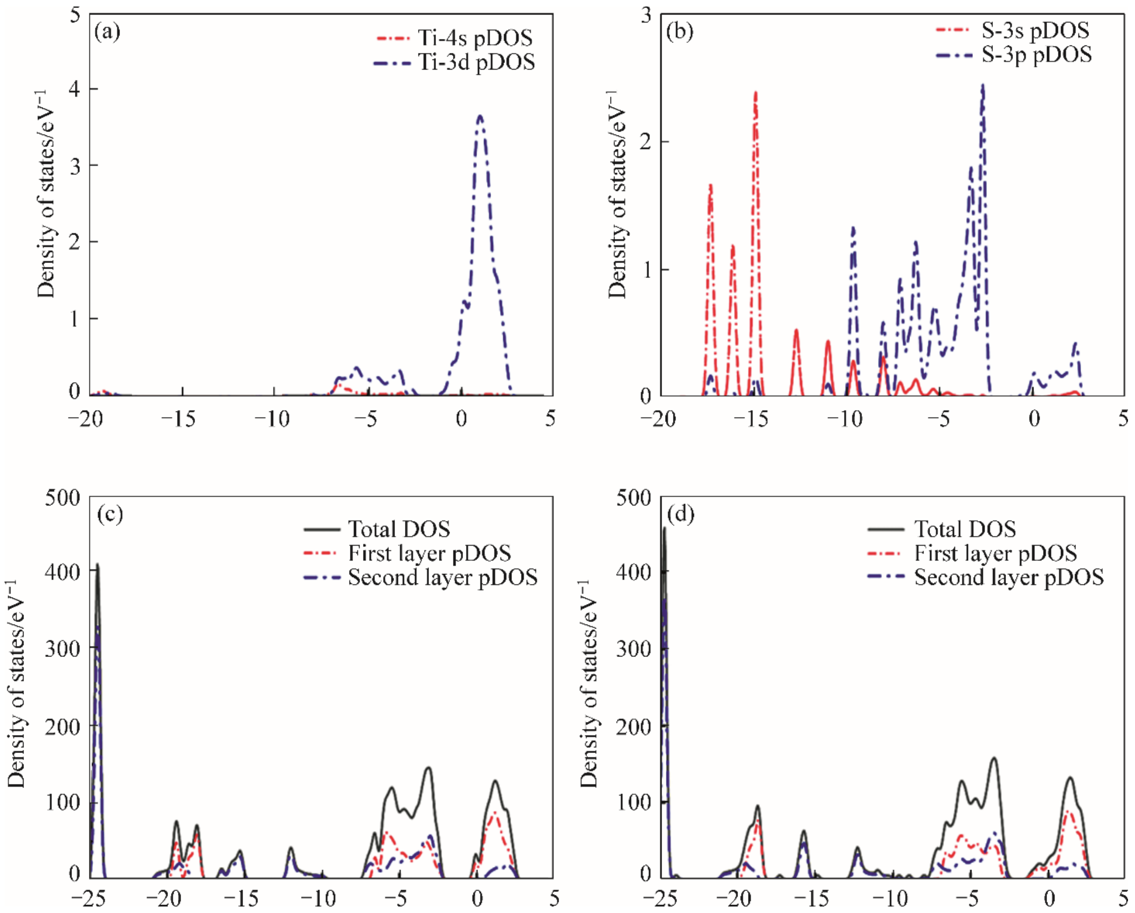

Figure S12 pDOS curves of (a) Ti and (b) S; Total DOS curves of (c) unadsorbed and (d) adsorbed of BT and corresponding pDOS curves of first layer and second layer

Table S1 Pore textural properties of composites

Sample	$S_{\mathrm{BET}}/(\mathrm{m^2 \cdot g^{-1}})^a$	$V/(\mathrm{cm^3 \cdot g^{-1}})^b$	d/nm^c
T	40.02	0.25	18.48
B	13.81	0.05	3.39
BT	35.23	0.19	18.28
AuT	56.90	0.32	18.13
AuB	14.34	0.04	3.07
AuBT-3	43.29	0.22	18.26

Note: ^{a} BET specific surface area; ^{b} BJH desorption cumulative volume of pores; ^{c} BJH desorption average pore diameter.

Table S2 Comparison of the degradation efficiency of previously reported photocatalysts used for photocatalytic degradation of xanthates

Photocatalyst	Light source	Pollutant	Dosage/ ($mg \cdot L^{-1}$)	Degradation rate/%	Irradiation time/min	Ref.
CdS/PANI/MWCNTs	Mercury lamp	SBX	30	99.20	70	[1]
TiO_2/clinoptilolite	Mercury lamp	SIPX	20	Over 90	30	[2]
BiOCl/TiO_2/clinoptilolite	Xe lamp	SIPX	20	91.20	180	[3]
TiO_2/graphene	Xe lamp	PBX	20	97.03	100	[4]
TiO_2/g-C_3N_4	Xe lamp	PBX	20	97.10	100	[5]
Fe(III)/Hydroxyapatite	Xe lamp	PBX	20	94.10	180	[6]
graphite/BiOI	Xe lamp	SIPX	50	94.36	125	[7]
Ag/TiO_2/clinoptilolite	Xe lamp	SIPX	20	~60	180	[8]
AuBT	Xe lamp	SEX	20	95.20	20	This work

Note: PBX: potassium butyl xanthate; SIBX: sodium isobutyl xanthate.

Table S3 Chemical structures and *m*/*z* values of possible degradation intermediates of SEX

Item	$C_3H_5O_2S^-$	$C_2H_3O_3S_2^-$	$C_4H_5OS_4^-$
Molecular structure	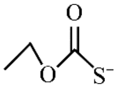	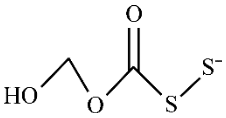	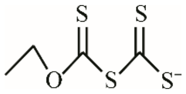
Molecular weight	105	139	197
m/*z*	105.2	141.4	198.1, 199.1

References

[1] JIA Yun, ZHANG Yu, ZHANG Xuan, et al. Novel CdS/PANI/MWCNTs photocatalysts for photocatalytic degradation of xanthate in wastewater [J]. Separation and Purification Technology, 2023, 309: 123022. DOI: 10.1016/j.seppur.2022.123022.

[2] SHEN Yan-bai, ZHOU Peng-fei, ZHAO Si-kai, et al. Synthesis of high-efficient TiO_2/clinoptilolite photocatalyst for complete degradation of xanthate [J]. Minerals Engineering, 2020, 159: 106640. DOI: 10.1016/j.mineng.2020.106640.

[3] ZHOU Peng-fei, SHEN Yan-bai, ZHAO Si-kai, et al. Synthesis of clinoptilolite-supported BiOCl/TiO_2 heterojunction nanocomposites with highly-enhanced photocatalytic activity for the complete degradation of xanthates under visible light [J]. Chemical Engineering Journal, 2021, 407: 126697. DOI: 10.1016/j.cej.2020.126697.

[4] JIANG Man, ZHANG Ming-hui, WANG Long-zhen, et al. Photocatalytic degradation of xanthate in flotation plant tailings by TiO_2/graphene nanocomposites [J]. Chemical Engineering Journal, 2022, 431: 134104. DOI: 10.1016/j.cej.2021.134104.

[5] ZHANG Ming-hui, HAN Ning, FEI Ya-wen, et al. TiO_2/g-C_3N_4 photocatalyst for the purification of potassium butyl xanthate in mineral processing wastewater [J]. Journal of Environmental Management, 2021, 297: 113311. DOI: 10.1016/j.jenvman.2021.113311.

[6] SHU Kai-qian, CHUAICHAM C, NOGUCHI Y, et al. In-situ hydrothermal synthesis of Fe-doped hydroxyapatite photocatalyst derived from converter slag toward xanthate photodegradation and Cr(VI) reduction under visible-light irradiation [J]. Chemical Engineering Journal, 2023, 459: 141474. DOI: 10.1016/j.cej.2023.141474.

[7] ZHENG Yu-fei, YUAN Fei, GAO Deng-zheng, et al. Improved visible-light-driven activity of micro graphite/BiOI nanocomposite for effective removal of xanthate from wastewater [J]. Materials Research Bulletin, 2023, 158: 112080. DOI: 10.1016/j.materresbull.2022.112080.

[8] ZHOU Peng-fei, SHEN Yan-bai, ZHAO Si-kai, et al. Facile synthesis of clinoptilolite-supported Ag/TiO_2 nanocomposites for visible-light degradation of xanthates [J]. Journal of the Taiwan Institute of Chemical Engineers, 2021, 122: 231−240. DOI: 10.1016/j.jtice.2021.04.049.

[9] PERDEW J P, CHEVARY J A, VOSKO S H, et al. Atoms, molecules, solids, and surfaces: Applications of the generalized gradient approximation for exchange and correlation [J]. Physical Review B-Condensed Matter, 1992, 46(11): 6671−6687. DOI: 10.1103/physrevb.46.6671.

[10] PERDEW J P, WANG Yue. Accurate and simple analytic representation of the electron-gas correlation energy [J]. Physical Review B, 1992, 45(23): 13244−13249. DOI: 10.1103/physrevb.45.13244.

[11] HUJO W, GRIMME S. Comparison of the performance of dispersion-corrected density functional theory for weak hydrogen bonds [J]. Physical Chemistry Chemical Physics, 2011, 13(31): 13942−13950. DOI: 10.1039/C1CP20591A.

[12] VANDERBILT D. Soft self-consistent pseudopotentials in a generalized eigenvalue formalism [J]. Physical Review B, 1990, 41(11): 7892−7895. DOI: 10.1103/physrevb.41.7892.